ACS APPLIED MATERIALS & INTERFACES

Research Article

Cite This: ACS Appl. Mater. Interfaces XXXX, XXX, XXX-XXX

www.acsami.org

Green Fabrication of Ultrathin Co_3O_4 Nanosheets from Metal–Organic Framework for Robust High-Rate Supercapacitors

Zhenyu Xiao,[†,§] Lili Fan,[†,§] Ben Xu,[†] Shanqing Zhang,*[,‡] Wenpei Kang,[†] Zixi Kang,[†] Huan Lin,[†] Xiuping Liu,[†] Shiyu Zhang,[†] and Daofeng Sun*[,†]

[†]State Key Laboratory of Heavy Oil Processing, College of Science, China University of Petroleum (East China), Qingdao Shandong 266580, People's Republic of China

[‡]Centre for Clean Environment and Energy, Griffith School of Environment, Gold Coast Campus, Griffith University, Southport, QLD 4222, Australia

Supporting Information

ABSTRACT: Two-dimensional cobalt oxide (Co_3O_4) is a promising candidate for robust electrochemical capacitors with high performance. Herein, we use 2,3,5,6-tetramethyl-1,4-diisophthalate as a recyclable ligand to construct a Co-based metal–organic framework of **UPC-9**, and subsequently, we obtain ultrathin hierarchical Co_3O_4 hexagonal nanosheets with a thickness of 3.5 nm through a hydrolysis and calcination process. A remarkable and excellent specific capacitance of 1121 $F{\cdot}g^{-1}$ at a current density of 1 $A{\cdot}g^{-1}$ and 873 $F{\cdot}g^{-1}$ at a current density of 25 $A{\cdot}g^{-1}$ were achieved for the as-prepared asymmetric supercapacitor, which can be attributed to the ultrathin 2D morphology and the rich macroporous and mesoporous structures of the ultrathin Co_3O_4 nanosheets. This synthesis strategy is environmentally benign and economically viable due to the fact that the costly organic ligand molecules are recycled, reducing the materials cost as well as the environmental cost for the synthesis process.

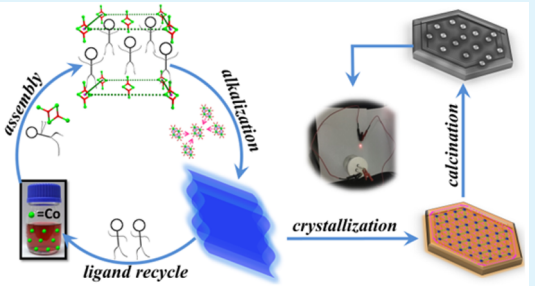

KEYWORDS: *Co_3O_4 nanosheets, $Co(OH)_2$ nanosheets, metal–organic framework, supercapacitor, eco-friendly, self-assembly*

INTRODUCTION

The pursuit of sustainable and renewable energy storage and conversion technologies is of importance to address the severe energy crisis worldwide.[1−3] Supercapacitors are an ideal solution to it because of their high power densities, fast recharge capability, and long cycle lifes.[4−7] Supercapacitors are classified into two categorizes based on their energy storage principles: electrical double-layer capacitance (EDLC) and pesudocapacitance.[8,9] For EDLC, although fast response to potential changes and high power density can be achieved, the energy density is relatively low because only the surface of the electrode materials is activated. Pseudocapacitance is associated with the reversible redox reactions, intercalation, or electrosorption at or near the active material surface. Therefore, the pseudocapacitance can be as large as 10 times of EDLC for some transition metal oxides and hydroxides.

Among the candidates for pseudocapacitor electrodes, Co_3O_4 is one of the most attractive options due to its high theoretical specific capacitance (ca. 3560 $F{\cdot}g^{-1}$), good electrochemical stability, low cost, and environmental friendliness.[10−12] In order to achieve better electrochemical performances, Co_3O_4 materials with various structures/morphologies, such as nanotubes, fibers, nanoflowers, nanospheres, nanocages, nanosheets, and wires, have been synthesized.[13−19] Most Co_3O_4 electrodes reported show specific capacitances below 1000 $F{\cdot}g^{-1}$, and the specific capacitances usually severely decay at high charge/discharge currents.[20−23] It is established that the Co_3O_4 electrodes with layered morphologies, especially an ultrathin nanosheet structure, deliver high electrochemical performance and stability because such morphologies provide abundant electrochemical active sites for direct electron transfer processes.[24−27] For example, Lou et al. synthesized ultrathin hierarchical Co_3O_4 nanosheet arrays on the Ni foam support, which showed an ultrahigh electrochemical capacitor value of 2735 $F{\cdot}g^{-1}$ at a current density of 2 $A{\cdot}g^{-1}$, and 53.7% of the supercapacitor maintained at a high current density of 10 $A{\cdot}g^{-1}$.[28] Therefore, the rational design and synthesis of layer-structured Co_3O_4 electrodes is of great significance to high performance supercapacitors.

Metal–organic frameworks (MOFs), constructed by alternatively connecting metal ions or metal clusters with organic ligands in a three-dimensional space, have been widely used as sacrificial precursors to synthesize porous metal oxide nanomaterials by pyrolysis methods.[29−33] Several specific MOFs are constructed by bridging the organic ligands together between the crystal layers, which is ideal for the preparation of laminar metal oxide materials.[34,35] However, there are two significant barriers that need to be overcome in order to produce the

Received: July 21, 2017
Accepted: November 7, 2017
Published: November 7, 2017

DOI: 10.1021/acsami.7b10309
ACS Appl. Mater. Interfaces XXXX, XXX, XXX−XXX

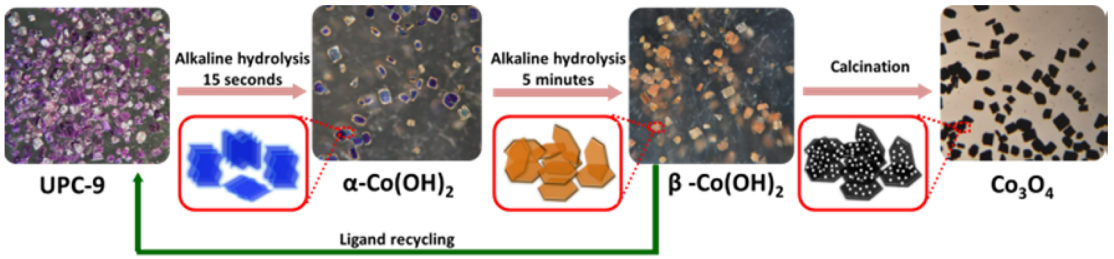

Figure 1. Phase transformation process of **UPC-9** and formation of ultrathin Co_3O_4 nanosheets.

layered metal oxide materials via this pathway. On one hand, the consumption of expensive organic ligands during the pyrolysis makes the resultant product extremely costly, accompanied by producing gaseous toxins. On the other hand, controlling the structure during pyrolysis processes is very difficult, causing inconsistent quality of the resultant products. For these reasons, the porous Co_3O_4 materials synthesized by pyrolysis commonly show unsatisfied electrochemical performances.[36] There is not an effective strategy to construct laminar Co_3O_4 nanomaterials with the capability in recycling ligands and inheriting the parent porosity by using MOFs as precursor so far.

Herein, using a Co-based MOFs (**UPC-9**) as precursor, we fabricate ultrathin Co_3O_4 nanosheets for application in supercapacitors. 3,5,6-Tetramethyl-1,4-diisophthalate is used as the ligand to react with the Co salt to prepare a Co-based MOF of **UPC-9**. The hydrolysis of **UPC-9** yields hexagonal $Co(OH)_2$ nanosheets, and subsequently, calcination of the $Co(OH)_2$ nanosheets produces a hierarchical structure fabricated by Co_3O_4 nanosheets. It is envisaged that the as-produced Co_3O_4 nanomaterial will deliver remarkable electrochemical performance if the layered structure is achieved. Moreover, the organic ligands in **UPC-9** dissolved in alkaline aqueous solution can be recycled through a simple acidization reaction. The resultant products are subject to systematic materials characterization to verify the proposed synthesis route while the performance is evaluated by a series of conventional electrochemical techniques. To our knowledge, the successful synthesis of ultrathin Co_3O_4 nanosheets using MOFs as precursors in a ligand-recyclable way has not been reported.

EXPERIMENTAL SECTION

Synthesis of UPC-9. A measured amount of $Co(NO_3)_2{\cdot}6H_2O$ (25 mg, 0.086 mmol) and H_4**L** (15 mg, 0.032 mmol) were dissolved in a 4 mL mixture of solvents (DMA/H_2O, v/v = 1:1), and the solution was sealed in a pressure-resistant Teflon-lined stainless container. The mixture was maintained at a temperature of 120 °C for 3 days after a gradual heating from room temperature in 2 h. Then, the reactor slowly dropped to room temperature in 5 h. Red-violet crystals were produced at the bottom of the container and were collected by filtration. The products were rinsed with fresh mother liquid and air-dried (yield: 85%, based on organic ligand).

Synthesis of $Co(OH)_2$. **UPC-9** was immersed in the aqueous solution of 1 M KOH for 1 h, and the crystal color gradually changed from bright-purple blue to pink in an outside-in process. The following measurements confirmed that the pink products were $Co(OH)_2$. The products were rinsed with deionized water and CH_3OH sequentially, absorbed KOH was removed, and the products were dried in vacuum at 65 °C for 10 h.

Synthesis of Co_3O_4. Co_3O_4 was synthesized by calcination of the $Co(OH)_2$. The $Co(OH)_2$ was heated to 350 °C at 20 °C intervals each minute, and maintained at 350 °C for 50 min. Black solids were produced and were confirmed to be Co_3O_4 by following measurements.

RESULTS AND DISCUSSION

Assembly of Hierarchical Co_3O_4 Nanosheet. Hierarchical Co_3O_4 nanosheets were fabricated through a two-step synthesis route from the MOF precursor of **UPC-9** which has layered arrangements. This unique structure is extremely suitable for transforming to layered porous $Co(OH)_2$ by controllably removing the bridged ligands, and the target Co_3O_4 products can be obtained in a relatively low temperature (350 °C), which is beneficial for preserving the morphology of $Co(OH)_2$. Moreover, dehydration during calcination of $Co(OH)_2$ will further increase the porosity of Co_3O_4 material.[37] Therefore, the hydrolysis and subsequent calcination of **UPC-9** is ideal for synthesis of layered Co_3O_4 with the high porosity.

Red-violet crystals of **UPC-9** were synthesized by the solvothermal reaction of $Co(NO_3)_2{\cdot}6H_2O$ and 2,3,5,6-tetramethyl-1,4-diisophthalate (denoted as H_4**L**) in the mixed solvents of DMA/H_2O (v/v = 1:1). The formula of **UPC-9** ($[Co_4(OH)_2(L)_{1.5}(H_2O)_4]{\cdot}3H_2O{\cdot}2.5DMA$) was further confirmed by elemental analysis, TGA, and X-ray single-crystal diffraction (crystallographic data can be seen in the Supporting Information, Table S1). Topologically, **UPC-9** possesses a *4,4,6T1* net based on a 4-connected organic linker (**L**) and a 6-connected $[Co_4(\mu_3\text{-}OH)_2(COO)_6]$ **SBU** (Supporting Information, Figure S2). Four cobalt ions are connected by two μ_3-OH groups and six carboxylate groups, forming a four-centered $[Co_4(\mu_3\text{-}OH)_2(COO)_6]$ **SBU** (**FC-SBU**).

The layered arrangement of **FC-SBUs** in **UPC-9** is the key to the hierarchical products. Instead of direct calcination, the hierarchical Co_3O_4 nanosheets are prepared in a two-step route. As shown in Figure 1, the fabrication route is the hydrolysis and subsequent calcination, and the chemical reactions are as shown:

$$2[Co_4(OH)_2(L)_{1.5}(H_2O)_4] + 12KOH \rightarrow 8Co(OH)_2 + 3K_4L + 8H_2O \quad (1)$$

$$6Co(OH)_2 + O_2 \rightarrow 2Co_3O_4 + 6H_2O \quad (2)$$

$$K_4L + 4HCl \rightarrow H_4L + 4KCl \quad (3)$$

$$3H_4L + 8Co(NO_3)_2 + 12H_2O \rightarrow 2[Co_4(OH)_2(L)_{1.5}(H_2O)_4] + 16HNO_3 \quad (4)$$

As is known, pyrolysis of MOFs usually causes aggregation of products due to the removal of organic ligands by oxidization.[36,38−40] Moreover, oxidation of organic ligands leads to elevated costs of production and hazards to environments, which is inappropriate for large-scaled applica-

DOI: 10.1021/acsami.7b10309
ACS Appl. Mater. Interfaces XXXX, XXX, XXX−XXX

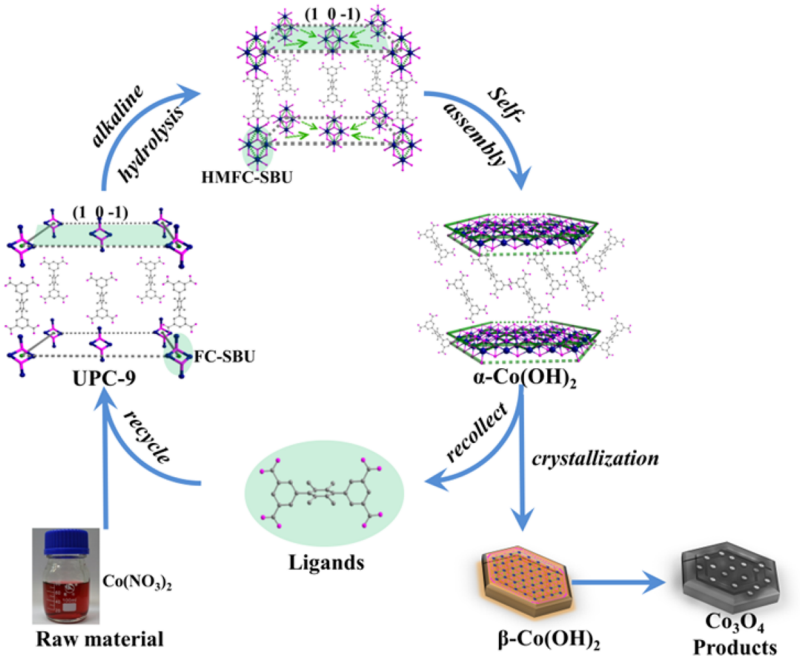

Figure 2. Schematic illustration of the transformation mechanism of **UPC-9**, α-$Co(OH)_2$, and β-$Co(OH)_2$.

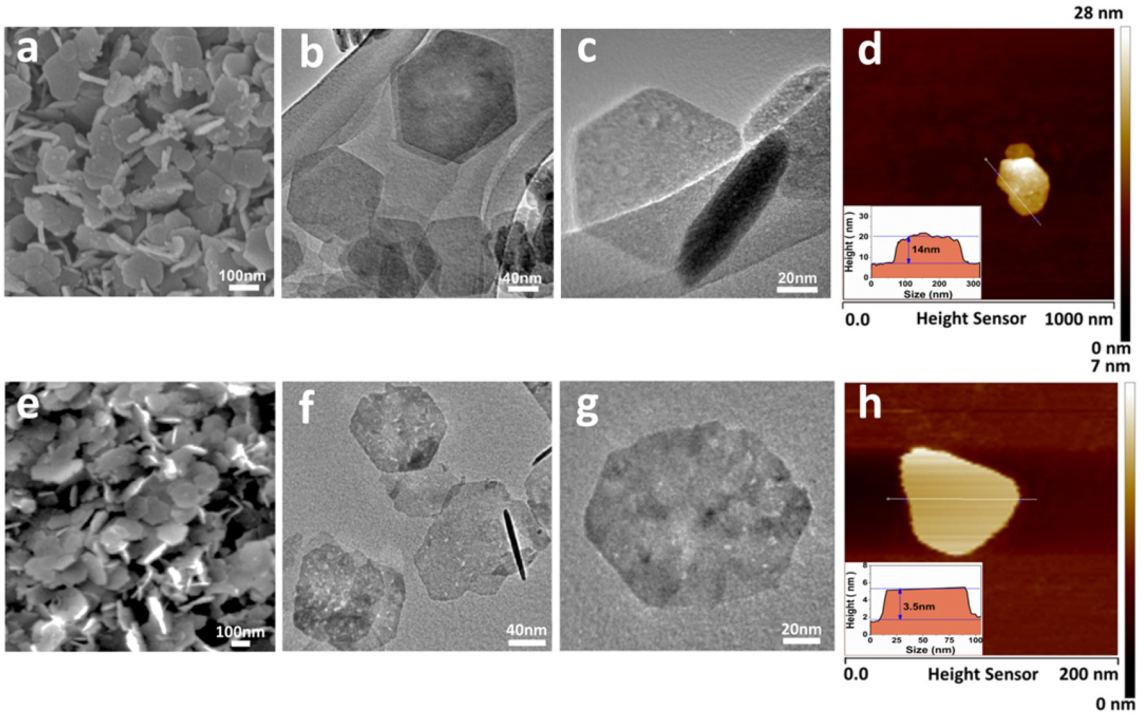

Figure 3. Morphological characterization of the $Co(OH)_2$ and Co_3O_4 samples at different scales: (a) SEM image of the $Co(OH)_2$ sample. (b, c) TEM images of the hexagonal $Co(OH)_2$ nanosheets with different magnification. (d) AFM image and the thickness analysis (the inset) of the $Co(OH)_2$ nanosheet. (e) SEM image of Co_3O_4 nanosheets. (f, g) TEM images of the Co_3O_4 nanosheets. (h) AFM image and the thickness analysis (the inset) of the Co_3O_4 nanosheet.

tion. We utilized a hydrolysis process to solve the issues. Unlike most MOF materials, hydrolysis of **UPC-9** does not break the pristine morphology but produces a hierarchical macrostructure of $Co(OH)_2$ nanosheets. Meanwhile, the ligands dissolved in alkaline aqueous solution can be easily recycled by simple neutralization, which efficiently solves the economic and environmental issues caused by traditional pyrolysis. By directly soaking **UPC-9** crystals in 1 M KOH solution, the red-violet **UPC-9** crystals instantly turned blue. Subsequently, a dramatic color change from blue to pink in 5 min was observed (Figure 1), implying the successful preparation of β-$Co(OH)_2$. The ligand can be recycled with a ratio of 85% and has high purity indicated by its ^{1}H NMR spectrum (Supporting Information, Figure S3), and the recycled ligand can be directly utilized for the preparation of **UPC-9** precursor for the next cycle.

DOI: 10.1021/acsami.7b10309
ACS Appl. Mater. Interfaces XXXX, XXX, XXX−XXX

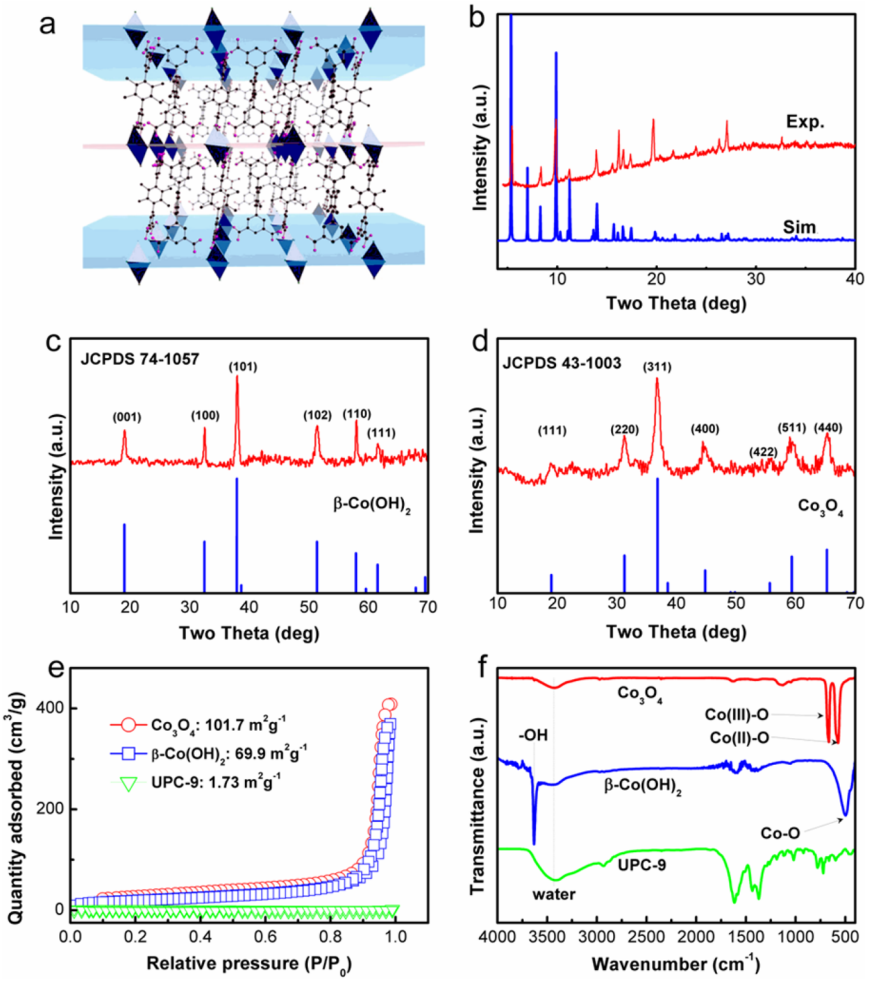

Figure 4. (a) 3D pillar–layer architecture of **UPC-9**. (b) Experimental (blue) and simulated (red) XRD patterns of **UPC-9**. (c, d) XRD patterns of $Co(OH)_2$ and Co_3O_4 compared with their standard JCPDS cards, respectively. (e) N_2 adsorption–desorption isotherms of **UPC-9**, $Co(OH)_2$, and Co_3O_4 measured at 77 K. (f) FTIR spectra of the **UPC-9**, $Co(OH)_2$, and Co_3O_4 nanosheets.

The specific feature of **UPC-9** to facilitate the production of the nanosheet morphology during hydrolysis can be explained as a hydroxyl-induced oriented reassembly of **FC-SBUs** (Figure 2). The hydrolysis of **UPC-9** can be classified into 3 steps. Once **UPC-9** crystals are immersed into the KOH aqueous solution, coordination bonds between metal clusters and carboxylate on crystal surface can readily react with hydroxyl ions (Supporting Information, Figure S4), resulting in hydroxyl-modified FC-SBUs (i.e., **HMFC-SBUs**) and free organic ligands (L^{4-}). Subsequently, the **HMFC-SBUs** crystallize in the (1 0 −1) plane and transform into 2D blue α-$Co(OH)_2$ with single atomic layers. The L^{4-} ions between **HMFC-SBUs** planes hamper the possible connection between adjacent **HMFC-SBUs**, which plays a critical role in the formation of α-$Co(OH)_2$ single atomic layers. In this way, the profile shape of **UPC-9** crystals is well preserved. After that, with continuous diffusion, hydroxyl ions gradually replace the L^{4-} ligands filling between α-$Co(OH)_2$ single layers, which induces phase transition from blue α-$Co(OH)_2$ to pink β-$Co(OH)_2$ nanosheets in the thickness of a few atoms. The residual L^{4-} ligands between α-$Co(OH)_2$ single layers prevent the aggregation to a great extent, which is beneficial to the formation of the hierarchical $Co(OH)_2$. The $Co(OH)_2$ can then be transformed into hierarchical Co_3O_4 nanosheets products by a subsequent calcination process at 350 °C for 50 min.

Structural Characterization of Hierarchical $Co(OH)_2$ and Co_3O_4 Nanosheets. In order to investigate the effect of synthesis route on the structural properties of final products, both $Co(OH)_2$ intermediates and Co_3O_4 products are examined using SEM, TEM, AFM, XRD, FTIR, and TGA methods. The morphologies of $Co(OH)_2$ were first examined by SEM and TEM (Figure 3a–c). Uniform sized $Co(OH)_2$ hexagonal nanosheets arrange in a hierarchical structure. A $Co(OH)_2$ nanosheet is 150 nm in width and 14 nm in thickness, and moreover, no cracks or secondary phases are observed, which indicates the good controllability of the hydrolysis process (Figure 3d). The hierarchical nanosheet structure is well preserved during the subsequent calcination. As shown in Figure 1, Co_3O_4 presents the similar macroscopic morphology as $Co(OH)_2$, implying the large porosity in the final products. The average diameter of Co_3O_4 nanosheets is similar as $Co(OH)_2$ but much narrower than the intermediates (Figure 3e). A Co_3O_4 nanosheet is only 3.5 nm thick and has large amounts of nanovoids which are expected to improve electrochemical performances (Figure 3f–h). We believe the shrinkage due to the dehydration of $Co(OH)_2$ in the calcination is responsible for the thinner nanosheets and nanovoids. XRD measurements were employed to provide the

DOI: 10.1021/acsami.7b10309
ACS Appl. Mater. Interfaces XXXX, XXX, XXX–XXX

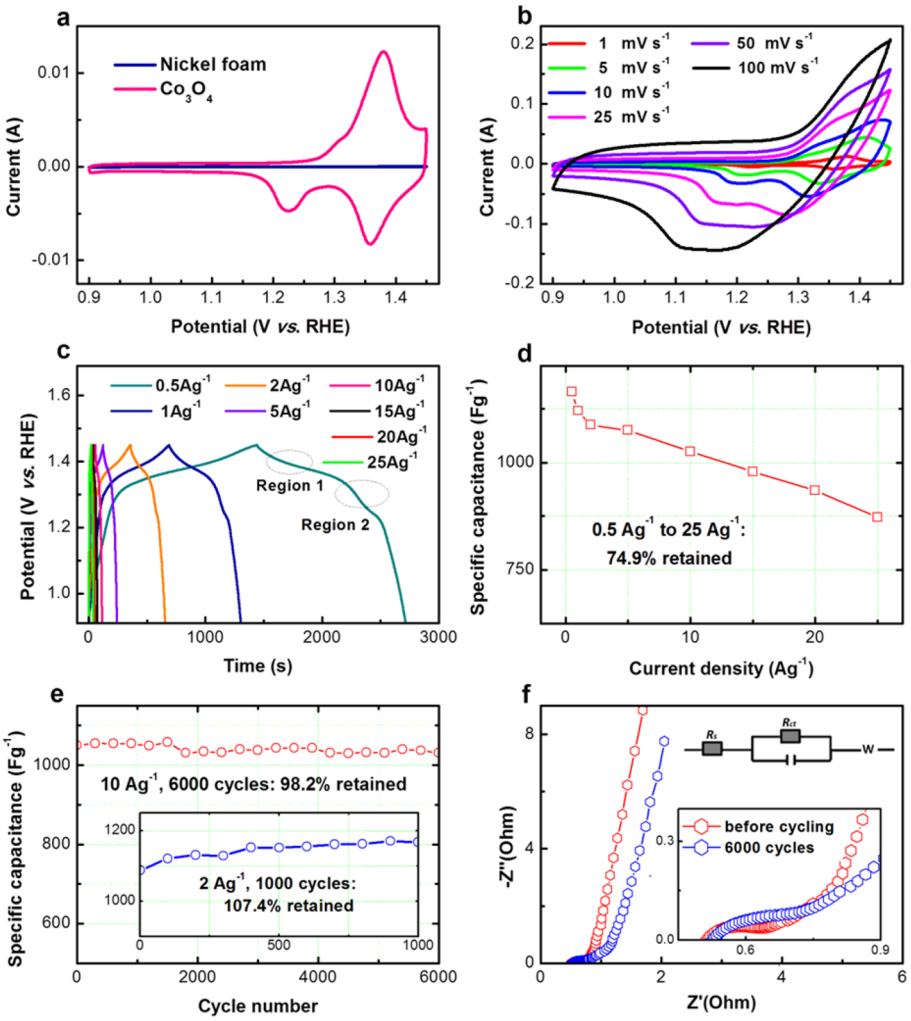

Figure 5. Electrochemical characterization of Co_3O_4. (a) Cyclic voltammograms of nickel foam (blue) and Co_3O_4 (pink) at scan rate of 1 mV s^{-1}. (b) CV curves at different scan rates. (c) Galvanostatic charge/discharge curves obtained at different current densities. (d) Corresponding specific capacitance as a function of current density. (e) Cycling performance at a charge/discharge current density of 10 A·g^{-1}. Inset: cycling performance at a charge/discharge current density of 2 A·g^{-1}. (f) Nyquist plots before and after 6000 cycles (the inset is the equivalent circuit model and the enlarged view of the high frequency region).

compositional information on precursors, intermediate, and products. **UPC-9** consisted of layer-arranged Co secondary building units (**SBUs**) and ligands as pillars in between (Figure 4a). As shown in Figure 4b, the well-resolved experimental PXRD pattern of the precursor **UPC-9** matches the simulated counterpart, indicating the single-phase **UPC-9** crystals. The XRD measurements confirm that the pink intermediates by alkaline hydrolyzing **UPC-9** are single-phase β-$Co(OH)_2$ (JCPDS card No. 74-1057). There are no further **UPC-9** peaks, suggesting the full transformation of the MOF precursor. The broad and weak peaks imply the nanosized $Co(OH)_2$ crystals, corresponding to the SEM results. The interplanar spacing of 0.23 nm measured from the HRTEM image (Figure S5c) is assigned to (101) planes, confirmed by the XRD peaks. The XRD patterns of Co_3O_4 products from calcination of $Co(OH)_2$ are confirmed by Co_3O_4 standards (JCPDS card No. 43-1003). As shown in Figure 4d, the weak peaks at the 2θ angles of 19°, 31°, 36.5°, 44.5°, 55.5°, 59°, and 65.5° are associated with the (111), (220), (311), (400), (422), (511), and (440) crystal planes, respectively. It suggests that all $Co(OH)_2$ transforms to Co_3O_4 since no extra peaks presented in the XRD patterns. The HRTEM image (Figure S5f) shows the well-resolved lattice fringes of Co_3O_4 with an interplanar spacing of 0.25 nm, corresponding to the (311) planes of cubic Co_3O_4. The selected-area electron diffraction (SAED) also confirms the well-defined diffraction rings, indicating their polycrystalline characteristics (Figure S6). FTIR analysis further indicates the proposed transformation process from **UPC-9** to Co_3O_4. As presented in Figure 4f, the peaks from 500 to 2000 cm^{-1} in the **UPC-9** spectrum are mainly from organic ligands. After hydrolysis, the spectrum presents typical $Co(OH)_2$ features, and the organic ligands in **UPC-9** are dissolved in alkaline aqueous and then recycled by acid treatment (as shown in reaction 3). The strong and broad band centered at 498 cm^{-1} can be attributed to Co-O stretch, and the weak peak around 973 cm^{-1} is Co-OH bending.[41] The strong and narrow peak at 3632 cm^{-1} is the O-H stretch band from $Co(OH)_2$. The weak and broad bands at 3386 and 1630 cm^{-1} are due to O-H stretch and bending of water. The FTIR spectrum of calcinated $Co(OH)_2$ indicates the successful preparation of Co_3O_4. Two strong bands centered at 667 and 575 cm^{-1} are attributed to Co^{2+} in a tetrahedral hole and Co^{3+} in an octahedral hole, respectively.[42] X-ray photoelectron spectros-

DOI: 10.1021/acsami.7b10309
ACS Appl. Mater. Interfaces XXXX, XXX, XXX−XXX

Table 1. Comparison of Selected Co_3O_4 Materials Reported for Supercapacitors

structure	capacitance ($F \cdot g^{-1}$)	current ($A \cdot g^{-1}$)	rate (%) at related current ($A \cdot g^{-1}$)
Co_3O_4 nanosheets grown on Ni foam[10]	2194	1	54.6% at 15
sub-3 nm Co_3O_4 nanofilms[11]	1400	1	91.1% at 8
dendrite-like Co_3O_4 derived by CPs[25]	207.8	0.5	36.1% at 6
porous hollow Co_3O_4 derived by ZIF-67[33]	1100	1.25	39.4% at 12.5
porous Co_3O_4 derived by Co-MOFs[35]	125.6	1	94.7% at 3
Co_3O_4 nano/micro superstructures[45]	208	1	49% at 3
mesoporous Co_3O_4 derived by CPs[46]	427	1.25	61.1% at 7.5
porous Co_3O_4 nanowires[47]	260	2	65.7% at 15
macro-/mesoporous Co_3O_4[48]	742.3	0.5	60% at 20
brush-like Co_3O_4[49]	407.5	1	78.5% at 6
Co_3O_4 hollow tube[50]	1498	0.5	53% at 10
porous Co_3O_4 nanoflakes@SrGO[51]	406	1	80% at 16
3D Co_3O_4-RGO aerogel[52]	660	0.5	75.7% at 10
UPC-9 derived Co_3O_4 (our work)	1121	1	77.9% at 25

copy (XPS) results (Figure S7) were performed to illustrate the chemical compositions in Co_3O_4 products.

The deconvolution of the Co 2*p* fine spectra was achieved by fitting to six bands. Peaks at 780.9 and 796.2 eV are associated with the Co^{3+} ion, and the other two peaks at 779.4 and 794.6 eV are ascribed to the Co^{2+} ion. These four bands indicate the coexistence of divalent and trivalent cobalt ions. Two weak and broad satellites are also observed. The specific surfaces areas of **UPC-9** precursor, Co(OH) intermediate, and Co_3O_4 products were determined by their N_2 adsorption/desorption isotherms measured using Brunauer–Emmett–Teller (BET) methods at 77 K (Figure 4e). The specific surface area of Co_3O_4 is 101.7 $m^2 \cdot g^{-1}$, which far exceeds that of $Co(OH)_2$ (69.9 $m^2 \cdot g^{-1}$) and **UPC-9** (1.73 $m^2 \cdot g^{-1}$). This enlarged surface area also verifies the presence of nanovoids due to the volume shrinkage and dehydration during calcination.[37]

Electrochemical Activity Evaluation. To demonstrate the structural advantages of ultrathin Co_3O_4 nanosheets as pseudocapacitive materials, cyclic voltammetry (CV) and galvanostatic charge/discharge measurements of the prepared Co_3O_4 electrode with 2 mg of active materials were first performed in a three-electrode system using 6 M KOH aqueous solution as the electrolyte. Cyclic voltammetry (CV) plots (see Figure 5a,b) present typical pseudocapacitance features with the potential window from 0.9 to 1.45 V (vs RHE) at different scan rates. Faradaic reactions between Co^{4+}, Co^{3+}, and Co^{2+} contribute to the intensive redox peaks (as shown in the Supporting Information). The current peak intensities increase with increasing scan rates from 1 to 100 $mV \cdot s^{-1}$, suggesting its good reversibility of fast charge/discharge response (Figure 5b). It is also noted that the nickel foam has no contribution to specific capacitance (Figure 5a). Galvanostatic charge/discharge plots at the current density from 0.5 to 25 $A \cdot g^{-1}$ are shown in Figure 5c. Two inflexions can be observed at either charge or discharge route as circled. Region 1 corresponds to the Co^{4+}/Co^{3+} conversion and region 2 to the Co^{3+}/Co^{2+} conversion, corresponding to the previously reported results of Co_3O_4 electrodes.[43] The specific capacitances at different current densities were calculated based on the following equation[44]

$$C = (I \times \Delta t)/(m \times \Delta V) \quad \text{(I)}$$

where C, I, Δt, m, and ΔV are specific capacitance, current density, charging–discharging time, mass of pesudocapacitance materials, and potential window, respectively. The specific capacitances at different current densities are shown in Figure 5d. The pesudocapacitive material of hierarchical Co_3O_4 nanosheets exhibits the high specific capacitance value of 1121 $F \cdot g^{-1}$ at the current density of 1 $A \cdot g^{-1}$. Moreover, the excellent rate capability was also achieved at the current density as large as 25 $A \cdot g^{-1}$. The capacitance retention can be maintained as high as 77.9% (from 1121 $F \cdot g^{-1}$ at 1 $A \cdot g^{-1}$ to 873 $F \cdot g^{-1}$ at 25 $A \cdot g^{-1}$). The supercapacitor performance obtained in this work surpasses the previously reported MOF-derived metal hyro-/oxide electrodes, and most of the reported porous cobalt-based nanomaterials (Table 1). It is believed that the rich meso/macropore structure in hierarchical Co_3O_4 is the key to its excellent electrochemical properties, which enables a large amount of pesudocapacitive materials involving into the redox reactions and elevates specific capacitance. Moreover, the high porosity of this unique hierarchical structure provides numerous electrolyte reservoirs, which facilitates the fast diffusion of OH^- ions, and thus, good ratability at higher current densities.

Cycling stability is another important property that needs to be considered for practical application. The cycling stability of the Co_3O_4 pesudocapacitive electrode was examined within 1000 cycles at the constant current density of 2 $A \cdot g^{-1}$. The activation process, in which the specific capacitance values increase obviously with cycling times during the initial 600 cycles (from 1087.3 to 1154.5 $F \cdot g^{-1}$), is observed. This is common for a pesudocapacitor electrode due to that it usually requires several cycles to improve the electrode surface wettability and electrolyte ion accessibility, and thus an increment in specific capacitance usually occurs at the beginning. However, it is challenging to maintain the specific capacitance because of decay of activated materials during the repeated charge/discharge process. One common method to improve the cycling performance is hybridization of pesudocapacitive materials, such as wrapping activated materials with polymer to prevent degradation. Although the cycling stability is improved, the synthesis cost usually elevates and hinders the practical applications. Herein, we did not further modify the Co_3O_4 material by hybridization, but it still shows impressive cycling stability. As shown in Figure 5e, the specific capacitance maintains in the range of 1154.5–1167.3 $F \cdot g^{-1}$, from 600 to 1000 cycles at the charge/discharge current of 2 $A \cdot g^{-1}$. The cycling behavior was further examined at a higher charge/discharge rate (10 $A \cdot g^{-1}$) and for more cycling periods. The result is similar to that at 2 $A \cdot g^{-1}$. Only 1.81% capacitance fades during the long-term cycles at the high charge/discharge rate,

DOI: 10.1021/acsami.7b10309
ACS Appl. Mater. Interfaces XXXX, XXX, XXX–XXX

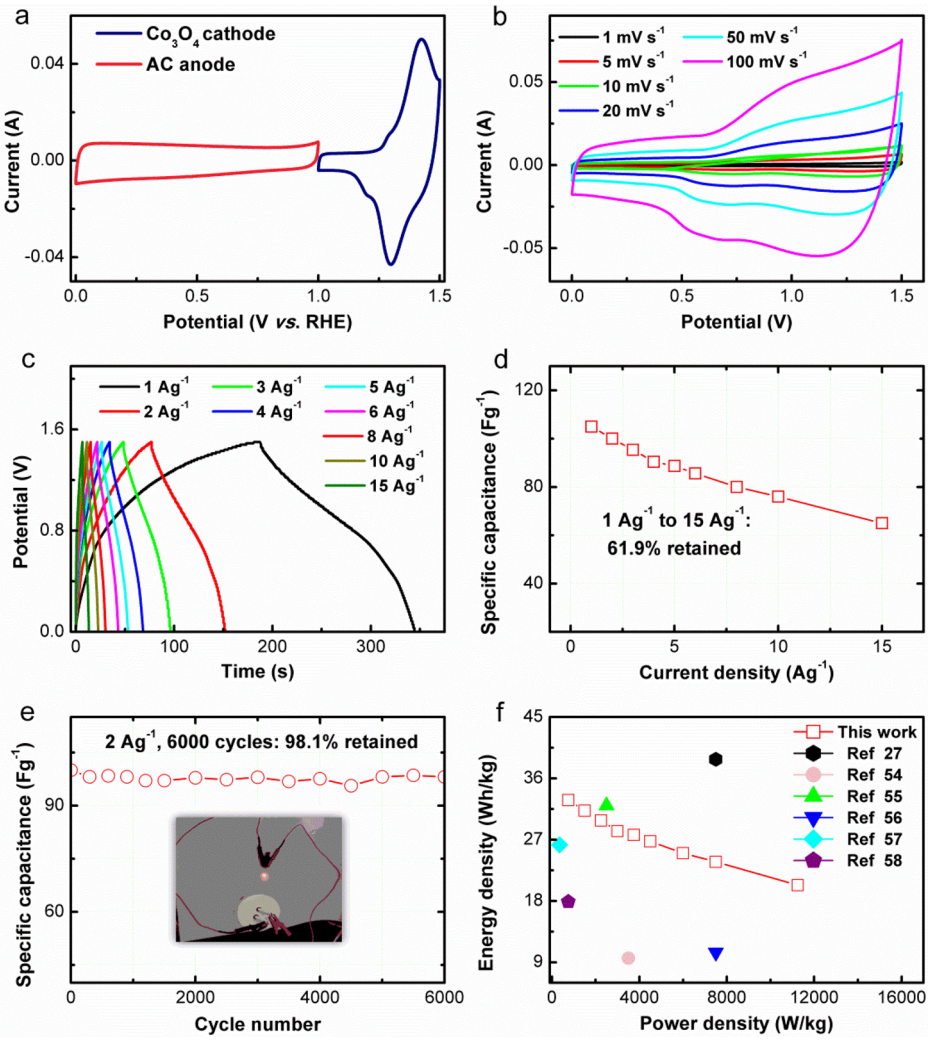

Figure 6. Electrochemical characterization of Co_3O_4//AC asymmetric supecapacitor. (a) CV curves of AC and the hierarchical Co_3O_4 at a scan rate of 10 mV s^{-1}. (b) CV curves at different scan rates. (c) GCD curves obtained at different current densities. (d) The specific capacitance vs current density. (e) Cycling performance at a current density of 2 A·g^{-1}. Inset: photograph of a red round LED indicator powered by two of our asymmetric supercapacitors. (f) Ragone plots of the Co_3O_4//AC asymmetric supercapacitor compared with previously reported results.

indicating the good pesudocapacitive behavior for potential applications. To track the morphology of the Co_3O_4 electrode at different cycling times, the electrode and the active materials peeled off from the electrode were checked by SEM analysis. As shown in Figures S8–S10, the Co_3O_4 nanosheets can keep their morphology after long-term cycling, contributing to the high cycling performance. The initial and last 12 galvanostatic charge–discharge cycles of the Co_3O_4 electrode at 2 and 10 A·g^{-1} are shown in Figures S11–S14, respectively, which also clearly illustrate that the charge–discharge process of the electrode is highly reversible.

Cycling stability of the Co_3O_4 was further investigated by Nyquist measurements at 1.25 V (vs RHE) over a frequency range of 0.01 Hz to 100 kHz. The Nyquist plots of the Co_3O_4 electrode before and after 6000 cycles are presented in Figure 5f. The *x*-intercept, radius circle, and the slope at the Warburg region on the Nyquist plot indicate the equivalent series resistance, charge transfer resistance, and ion diffusion resistance, respectively. The equivalent cyclic circuit for fitting is inserted in Figure 5f, and the corresponding parameters of the proposed equivalent circuit model are listed in Table S3. Both phases have angles that are close to 90° along the imaginary axis (Z″) before and after long-time cycling, indicating typical capacitance behaviors. In the medium frequency area (0.38 Hz for the phase angle of 45°), the angles between the inclined lines and the real axes are between 45° and 90°, corresponding to the ion diffusion mechanism between Warburg diffusion and ideal capacitive ion diffusion (pseudocapacitance). The equivalent series resistance is due to the ion diffusion in electrolyte, and does not change before and after cycling. The transfer resistance at the interface between electrolyte and electrode most increases, indicating the decay of active materials. However, the transfer resistance is still much smaller than the *x*-intercept even after long-term cycles, implying that the specific capacitance is mainly affected by electrolyte, which partly explains the good cycling stability of hierarchical Co_3O_4.

The high-rate capability and excellent reversibility are attributed to the following reasons: (1) The open geometry built by Co_3O_4 nanosheets is highly accessible to the electrolyte, which would decrease the electrolyte starvation near the electrode surface and facilitate ionic diffusion in the solid electrode, resulting in lower internal resistance and faster kinetics; (2) the large active surface area of Co_3O_4 can be

DOI: 10.1021/acsami.7b10309
ACS Appl. Mater. Interfaces XXXX, XXX, XXX–XXX

beneficial to electrolyte contact and adsorption of alkali ions, leading to capacitance improvement; (3) the as-synthesized Co_3O_4 nanosheets are ultrathin (with only a few nanometers in thickness) which ensures the maximum participation in the Faradaic reactions from outside to inside, and therefore facilitates a higher capacitance for charge storage; and (4) the unique structure of the Co_3O_4 nanosheets helps alleviate structural damages caused by volume change during the repetitive redox cycles, keeping structural integrity and providing better reversibility and cycling performance.

An asymmetric supercapacitor with hierarchical Co_3O_4 nanosheets as positive electrode and active carbon (AC) as negative electrode was fabricated in 6 M KOH solution in order to evaluate the practical application. The AC electrode was prepared by mixing 90 wt % of the activated carbon and 10 wt % of polytetrafluoroethylene and then spread onto a 1 cm × 2 cm Ni foam. Its specific capacitance is 140 $F{\cdot}g^{-1}$ at the current density of 2 $A{\cdot}g^{-1}$ (as shown in Figure S15). It is noted that the supercapacitive behavior of the AC electrode is typical EDLC, as illustrated by the rectangular CV curve shown in Figure 6a. Mass ratio between Co_3O_4 and AC was carefully calculated based on charge balance theory, $C^-\Delta V^- m^- = C^+\Delta V^+ m^+$,[53] for complete utilization of active materials and was optimized to 3.9:1.

Supercapacitor performances at different scan rates from 1 to 100 $mV{\cdot}s^{-1}$ were examined by CV plots. Two redox peaks are observed, which are much broader than those in the plots measured from the three electrode system. Galvanostatic charge/discharge curves of the asymmetric supercapacitor device at the current densities from 1 to 15 $A{\cdot}g^{-1}$ are demonstrated in Figure 6c. The specific capacitance ($F{\cdot}g^{-1}$), energy density ($W{\cdot}h{\cdot}kg^{-1}$), and the power density ($W{\cdot}kg^{-1}$) are then obtained from the following equations

$$C_t = (I \times \Delta t)/(m_t \times \Delta V) \quad \text{(II)}$$

$$E = 0.5 \times C_t \times \Delta V^2 \quad \text{(III)}$$

$$P = E \times \Delta t^{-1} \quad \text{(IV)}$$

where C_t is the total specific capacitance of an asymmetric supercapacitor, I is the charge/discharge current density, m_t is the total mass of cathode and anode active materials, Δt is the discharging time, and ΔV is the operating voltage window.

The specific capacitance reaches 105 $F{\cdot}g^{-1}$ at the current density of 1 $A{\cdot}g^{-1}$ and remains as high as 65 $F{\cdot}g^{-1}$ at the higher current density of 15 $A{\cdot}g^{-1}$, implying the good rate performance (as shown in Figure 5d). Furthermore, the Co_3O_4//AC asymmetric supercapacitor exhibits an extremely high energy density of 32.8 $W{\cdot}h{\cdot}kg^{-1}$ at the power density of 752 $W{\cdot}kg^{-1}$. Even at the high power density of 11248 $W{\cdot}kg^{-1}$, the supercapacitor still has a high energy density of 20.3 $W{\cdot}h{\cdot}kg^{-1}$, highlighting the rate capability of our asymmetric supercapacitor. To better illustrate the good specific energy and power densities in our asymmetric capacitor, a Ragone plot (Figure 6f) showing energy density versus power density for various asymmetric supercapacitors was made.[54−58] Our asymmetric supercapacitor clearly presents better performances, indicating the promising potential applications as devices. The superior performance is attributed to the high energy contribution of the Co_3O_4 positive electrode of the unique hierarchical porous structure.

Furthermore, a simple application to power a commercial light-emitting diode (LED) is demonstrated by our supercapacitor. The red LED (working voltage 1.6−3.0 V, 20 mA) was lighted up by charging the supercapacitor to 1.8 V at 2 $A{\cdot}g^{-1}$. Cycling performances of the asymmetric supercapacitor were also evaluated at the current density of 2 $A{\cdot}g^{-1}$. As shown in Figure 6e, a very small decrease of the capacitance is observed, which may be resulted from the consumption of the active materials caused by harsh redox reactions. After 6000 cycles, the device still maintains approximately 98.1% of its initial capacitance (initial 100 $F{\cdot}g^{-1}$, final 98.1 $F{\cdot}g^{-1}$), which demonstrates the excellent cycling stability and superiority to many previously reported asymmetric supercapacitors.[59−62] The initial and final 6 galvanostatic charge/discharge curves show little differences as shown in Figures S13 and S14, which demonstrates the excellent cycling stability. This stability performance is similar to that of the positive Co_3O_4 electrode.

CONCLUSION

In summary, a green fabrication method for ultrathin Co_3O_4 nanosheets is developed using the Co-based MOF of **UPC-9** as the sacrificial precursor by the hydrolysis and subsequent calcination process. The recycling of organic ligands during synthesis can drastically reduce the cost of materials and environmental hazards, offering a green manufacturing of functional nanomaterials. The as-prepared Co_3O_4 nanosheets present remarkable supercapacitor performance due to the plentiful meso- and macropores in the designed hierarchical structure The fabricated Co_3O_4/AC asymmetric supercapacitor exhibits a high energy density of 32.8 $W{\cdot}h{\cdot}kg^{-1}$ at the power density of 752 $W{\cdot}kg^{-1}$ and remains 98.1% of its initial capacitance after 6000 charge/discharge cycles at the current density of 2 $A{\cdot}g^{-1}$, indicating its impressive long-term cycling stability.

ASSOCIATED CONTENT

Supporting Information

The Supporting Information is available free of charge on the ACS Publications website at DOI: 10.1021/acsami.7b10309.

The synthesis methods, test methods and related characterization, the description of crystal of $Co(OH)_2$ and **UPC-9**, and the calculation of coordination motif transformation; SEM, HRTEM, and selected area electron diffraction spectra of **UPC-9** derived $Co(OH)_2$ and Co_3O_4; XPS of as-synthesized Co_3O_4; SEM of Co_3O_4 after different charge−discharge cycles; CV of Co_3O_4 electrode in range of 0.9−1.8 V; TGA, CV, GCD, and cycle performance of **UPC-9** derived $Co(OH)_2$; first 12 cycles and last 12 cycles GCD curves of Co_3O_4 electrode cycle test at different current density; H^1 NMR spectra of ligand and recycled ligand; table of specific capacitance, energy density and power density asymmetric supercapacitor; first 6 cycles and last 6 cycles GCD curves of asymmetric supercapacitor cycle test; GCD of AC electrode (PDF)

AUTHOR INFORMATION

Corresponding Authors

*E-mail: s.zhang@griffith.edu.au (S.Z.).
*E-mail: dfsun@upc.edu.cn (D.S.).

ORCID

Shanqing Zhang: 0000-0001-5192-1844
Daofeng Sun: 0000-0003-3184-1841

DOI: 10.1021/acsami.7b10309
ACS Appl. Mater. Interfaces XXXX, XXX, XXX−XXX

Author Contributions

[§]These authors contributed equally to this work.

Notes

The authors declare no competing financial interest.

■ ACKNOWLEDGMENTS

This work was supported by the NSFC (Grant Nos. 21371179, 21571187), NCET-11-0309, Taishan Scholar Foundation (ts201511019), and the Fundamental Research Funds for the Central Universities (13CX05010A, 14CX02150A, 15CX02069A, 15CX06074A).

■ REFERENCES

(1) Liu, J.; Galpaya, D. G. D.; Yan, L.; Sun, M.; Lin, Z.; Yan, C.; Liang, C.; Zhang, S. Exploiting a Robust Biopolymer Network Binder for an Ultrahigh-Areal-Capacity Li-S Battery. *Energy Environ. Sci.* **2017**, *10*, 750−755.

(2) Zhang, G.; Hou, S.; Zhang, H.; Zeng, W.; Yan, F.; Li, C. C.; Duan, H. High-Performance and Ultra-Stable Lithium-Ion Batteries Based on MOF-Derived ZnO@ZnO Quantum Dots/C Core-Shell Nanorod Arrays on a Carbon Cloth Anode. *Adv. Mater.* **2015**, *27*, 2400−2405.

(3) Zhang, Q.; Zhao, B.; Wang, J.; Qu, C.; Sun, H.; Zhang, K.; Liu, M. High-Performance Hybrid Supercapacitors Based on Self-supported 3D Ultrathin Porous Quaternary Zn-Ni-Al-Co Oxide Nanosheets. *Nano Energy* **2016**, *28*, 475−485.

(4) Sugimoto, W.; Iwata, H.; Yasunaga, Y.; Murakami, Y.; Takasu, Y. Preparation of Ruthenic Acid Nanosheets and Utilization of Its Interlayer Surface for Electrochemical Energy Storage. *Angew. Chem., Int. Ed.* **2003**, *42*, 4092−4096.

(5) Pachfule, P.; Shinde, D.; Majumder, M.; Xu, Q. Fabrication of Carbon Nanorods and Graphene Nanoribbons from a Metal-Organic Framework. *Nat. Chem.* **2016**, *8*, 718−724.

(6) Dong, B.; Li, M.; Chen, S.; Ding, D.; Wei, W.; Gao, G.; Ding, S. Formation of g-C_3N_4 @$Ni(OH)_2$ Honeycomb Nanostructure and Asymmetric Supercapacitor with High Energy and Power Density. *ACS Appl. Mater. Interfaces* **2017**, *9*, 17890−17896.

(7) Mendoza-Sánchez, B.; Gogotsi, Y. Synthesis of Two-Dimensional Materials for Capacitive Energy Storage. *Adv. Mater.* **2016**, *28*, 6104−6135.

(8) Simon, P.; Gogotsi, Y. Materials for Electrochemical Capacitors. *Nat. Mater.* **2008**, *7*, 845−854.

(9) Gao, S.; Sun, Y.; Lei, F.; Liang, L.; Liu, J.; Bi, W.; Pan, B.; Xie, Y. Ultrahigh Energy Density Realized by a Single-Layer β-$Co(OH)_2$ All-Solid-State Asymmetric Supercapacitor. *Angew. Chem., Int. Ed.* **2014**, *53*, 12789−12793.

(10) Qiu, K.; Lu, Y.; Cheng, J.; Yan, H.; Hou, X.; Zhang, D.; Lu, M.; Liu, X.; Luo, Y. Ultrathin Mesoporous Co_3O_4 Nanosheets on Ni Foam for High-Performance Supercapacitors. *Electrochim. Acta* **2015**, *157*, 62−68.

(11) Feng, C.; Zhang, J.; He, Y.; Zhong, C.; Hu, W.; Liu, L.; Deng, Y. Sub-3 nm Co_3O_4 Nanofilms with Enhanced Supercapacitor Properties. *ACS Nano* **2015**, *9*, 1730−1739.

(12) Wang, X.; Yao, S.; Wu, X.; Shi, Z.; Sun, H.; Que, R. High Gas-Sensor and Supercapacitor Performance of Porous Co_3O_4 Ultrathin Nanosheets. *RSC Adv.* **2015**, *5*, 17938−17944.

(13) Bendi, R.; Kumar, V.; Bhavanasi, V.; Parida, K.; Lee, P. S. Metal Organic Framework-Derived Metal Phosphates as Electrode Materials for Supercapacitors. *Adv. Energy Mater.* **2016**, *6*, 1501833.

(14) Rumplecker, A.; Kleitz, F.; Salabas, A. E.; Schüth, F. Hard Templating Pathways for the Synthesis of Nanostructured Porous Co_3O_4. *Chem. Mater.* **2007**, *19*, 485−496.

(15) Meher, S. K.; Rao, G. R. Ultralayered Co_3O_4 for High-Performance Supercapacitor Applications. *J. Phys. Chem. C* **2011**, *115*, 15646−15654.

(16) Xu, J.; Gao, L.; Cao, J.; Wang, W.; Chen, Z. Preparation and Electrochemical Capacitance of Cobalt Oxide (Co_3O_4) Nanotubes as Supercapacitor Material. *Electrochim. Acta* **2010**, *56*, 732−736.

(17) Zhou, C.; Zhang, Y.; Li, Y.; Liu, J. Construction of High-Capacitance 3D CoO@ Polypyrrole Nanowire Array Electrode for Aqueous Asymmetric Supercapacitor. *Nano Lett.* **2013**, *13*, 2078−2085.

(18) Rumplecker, A.; Kleitz, F.; Salabas, A. E.; Schüth, F. Templating Pathways for the Synthesis of Nanostructured Porous Co_3O_4. Chem. Mater. *Chem. Mater.* **2007**, *19*, 485−496.

(19) Jiang, J.; Liu, J. P.; Huang, X. T.; Li, Y. Y.; Ding, R. M.; et al. General Synthesis of Large-Scale Arrays of One-Dimensional Nanostructured Co_3O_4 Directly on Heterogeneous Substrates. *Cryst. Growth Des.* **2010**, *10*, 70−75.

(20) Wang, Y.; Lei, Y.; Li, J.; Gu, L.; Yuan, H.; Xiao, D. Synthesis of 3D-Nanonet Hollow Structured Co_3O_4 for High Capacity Supercapacitor. *ACS Appl. Mater. Interfaces* **2014**, *6*, 6739−6747.

(21) Rakhi, R. B.; Chen, W.; Hedhili, M. N.; Cha, D.; Alshareef, H. N. , Enhanced Rate Performance of Mesoporous Co_3O_4 Nanosheet Supercapacitor Electrodes by Hydrous RuO_2 Nanoparticle Decoration. *ACS Appl. Mater. Interfaces* **2014**, *6*, 4196−4206.

(22) Qorbani, M.; Naseri, N.; Moshfegh, A. Z. Hierarchical Co_3O_4/$Co(OH)_2$ Nanoflakes as a Supercapacitor Electrode: Experimental and Semi-Empirical Model. *ACS Appl. Mater. Interfaces* **2015**, *7*, 11172−11179.

(23) Pang, H.; Gao, F.; Chen, Q.; Liu, R.; Lu, Q. Dendrite-like Co_3O_4 Nanostructure and Its Applications in Sensors, Supercapacitors and Catalysis. *Dalton T.* **2012**, *41*, 5862−5868.

(24) Wang, L.; Dong, Z. H.; Wang, Z. G.; Zhang, F. X.; Jin, J. Layered α-$Co(OH)_2$ Nanocones as Electrode Materials for Pseudocapacitors: Understanding the Effect of Interlayer Space on Electrochemical Activity. *Adv. Funct. Mater.* **2013**, *23*, 2758−2764.

(25) Wang, H.; Casalongue, H. S.; Liang, Y.; Dai, H. $Ni(OH)_2$ Nanoplates Grown on Graphene as Advanced Electrochemical Pseudocapacitor Materials. *J. Am. Chem. Soc.* **2010**, *132*, 7472−7477.

(26) Yu, G.; Hu, L.; Vosgueritchian, M.; Wang, H.; Xie, X.; McDonough, J. R.; Cui, X.; Cui, Y.; Bao, Z. Solution-Processed Graphene/MnO2 Nanostructured Textiles for High-Performance Electrochemical Capacitors. *Nano Lett.* **2011**, *11*, 2905−2911.

(27) Wang, X.; Xia, H.; Wang, X.; Gao, J.; Shi, B.; Fang, Y. Facile Synthesis Ultrathin Mesoporous Co_3O_4 Nanosheets for High-Energy Asymmetric Supercapacitor. *J. Alloys Compd.* **2016**, *686*, 969−975.

(28) Yuan, C.; Yang, L.; Hou, L.; Shen, L.; Zhang, X.; Lou, X. W. D. Growth of Ultrathin Mesoporous Co_3O_4 Nanosheet Arrays on Ni Foam for High-Performance Electrochemical Capacitors. *Energy Environ. Sci.* **2012**, *5*, 7883−7887.

(29) Wu, R.; Qian, X.; Yu, F.; Liu, H.; Zhou, K.; et al. MOF-Templated Formation of Porous CuO Hollow Octahedra for Lithium-Ion Battery Anode Materials. *J. Mater. Chem. A* **2013**, *1*, 11126−11129.

(30) Morozan, A.; Jaouen, F. Metal Organic Frameworks for Electrochemical Applications. *Energy Environ. Sci.* **2012**, *5*, 9269−9290.

(31) Wu, R.; Qian, X.; Rui, X.; Liu, H.; Yadian, B.; Zhou, K.; Wei, J.; Yan, Q.; Feng, X.; Long, Y.; Wang, L.; Huang, Y. Zeolitic Imidazolate Framework 67-Derived High Symmetric Porous Co_3O_4 Hollow Dodecahedra with Highly Enhanced Lithium Storage Capability. *Small* **2014**, *10*, 1932−1938.

(32) Salunkhe, R. R.; Tang, J.; Kamachi, Y.; Nakato, T.; Kim, J. H.; Yamauchi, Y. Asymmetric Supercapacitors Using 3D Nanoporous Carbon and Cobalt Oxide Electrodes Synthesized from a Single Metal-Organic Framework. *ACS Nano* **2015**, *9*, 6288−6296.

(33) Zhang, Y.; Wang, Y.; Xie, Y.-L.; Cheng, T.; Lai, W.-Y. Porous Hollow Co_3O_4 with Rhombic Dodecahedral Structures for High-Performance Supercapacitors. *Nanoscale* **2014**, *6*, 14354−14359.

(34) Zou, F.; Hu, X.; Li, Z.; Qie, L.; Hu, C.; Zeng, R.; Jiang, Y.; Huang, Y. MOF-Derived Porous ZnO/$ZnFe_2O_4$/C Octahedra with Hollow Interiors for High-Rate Lithium-Ion Batteries. *Adv. Mater.* **2014**, *26*, 6622−6628.

(35) Meng, F.; Fang, Z.; Li, Z.; Xu, W.; Wang, M.; Liu, Y.; Zhang, J.; Wang, W.; Zhao, D.; Guo, X. Porous Co3O4Materials Prepared by

DOI: 10.1021/acsami.7b10309
ACS Appl. Mater. Interfaces XXXX, XXX, XXX−XXX

Solid-State Thermolysis of a novel Co-MOF Crystal and Their Superior Energy Storage Performances for Supercapacitors. *J. Mater. Chem. A* **2013**, *1*, 7235−7241.
(36) Yang, Q.; Lu, Z.; Sun, X.; Liu, J. Ultrathin Co_3O_4 Nanosheet Arrays with High Supercapacitive Performance. *Sci. Rep.* **2013**, *3*, 3537.
(37) Lou, X. W.; Deng, D.; Lee, J. Y.; Feng, J.; Archer, L. A. Self-Supported Formation of Needlelike Co_3O_4 Nanotubes and Their Application as Lithium-Ion Battery Electrodes. *Adv. Mater.* **2008**, *20*, 258−262.
(38) Wu, M.; Hsu, W. Nickel Nanoparticles Embedded in Partially Graphitic Porous Carbon Fabricated by Direct Carbonization of Nickel-Organic Framework for High-Performance Supercapacitors. *J. Power Sources* **2015**, *274*, 1055−1062.
(39) Meng, W.; Chen, W.; Zhao, L.; Huang, Y.; Zhu, M.; Huang, Y.; Fu, Y.; Geng, F.; Yu, J.; Chen, X.; Zhi, C. Porous Fe_3O_4/Carbon Composite Electrode Material Prepared from Metal-Organic Framework Template and Effect of Temperature on Its Capacitance. *Nano Energy* **2014**, *8*, 133−140.
(40) Luo, J.; Zhong, W.; Zou, Y.; Xiong, C.; Yang, W. Metal-Organic Coordination Polymer to Prepare Density Controllable and High Nitrogen-Doped Content Carbon/Graphene for High Performance Supercapacitors. *ACS Appl. Mater. Interfaces* **2017**, *9*, 317−326.
(41) Xia, X.; Tu, J.; Zhang, Y.; Wang, X.; Gu, C.; Zhao, X. B.; Fan, H. J. High-Quality Metal Oxide Core/Shell Nanowire Arrays on Conductive Substrates for Electrochemical Energy Storage. *ACS Nano* **2012**, *6*, 5531−5538.
(42) Jha, A.; Rode, C. V. Highly Selective Liquid-Phase Aerobic Oxidation of Vanillyl Alcohol to Vanillin on Cobalt Oxide (Co_3O_4) Nanoparticles. *New J. Chem.* **2013**, *37*, 2669−2674.
(43) Wang, X.; Li, M.; Chang, Z.; Yang, Y.; Wu, Y.; Liu, X. Co_3O_4@MWCNT Nanocable as Cathode with Superior Electrochemical Performance for Supercapacitors. *ACS Appl. Mater. Interfaces* **2015**, *7*, 2280−2285.
(44) Wang, X.; Sumboja, A.; Lin, M.; Yan, J.; Lee, P. *S.* Enhancing Electrochemical Reaction Sites in Nickel-Cobalt Layered Double Hydroxides on Zinc Tin Xxide Nanowires: a Hybrid Material for an Asymmetric Supercapacitor Device. *Nanoscale* **2012**, *4*, 7266−7272.
(45) Zhang, F.; Hao, L.; Zhang, L.; Zhang, X. Solid-State Thermolysis Preparation of Co3O4 Nano/Micro Superstructures From Metal-Organic Framework for Supercapacitors. *Int. J. Electrochem. Sci.* **2011**, *6*, 2943−2954.
(46) Wang, R.; Kong, L.; Lang, J.; Wang, X.; Fan, S.; Luo, Y.; Kang, L. Mesoporous Co_3O_4 Materials Obtained from Cobalt-Citrate Complex and Their High Capacitance Behavior. *J. Power Sources* **2012**, *217*, 358−363.
(47) Wang, B.; Zhu, T.; Wu, H. B.; Xu, R.; Chen, J. S.; Lou, X. W. Porous Co_3O_4 Nanowires Derived from Long $Co(CO_3)_{0.5}(OH)\bullet 0.11H_2O$ Nanowires with Improved Supercapacitive Properties. *Nanoscale* **2012**, *4*, 2145−2149.
(48) Wang, X.; Sumboja, A.; Khoo, E.; Yan, C.; Lee, P. S. Cryogel Synthesis of Hierarchical Interconnected Macro-/Mesoporous Co_3O_4 with Superb Electrochemical Energy Storage. *J. Phys. Chem. C* **2012**, *116*, 4930−4935.
(49) Dam, D. T.; Lee, J. Three-Dimensional Cobalt Oxide Microstructures with Brush-Like Morphology Via Surfactant-Dependent Assembly. *ACS Appl. Mater. Interfaces* **2014**, *6*, 20729−20737.
(50) Li, J.; Zan, G.; Wu, Q. An Ultra-High-Performance Anode Material for Supercapacitors: Self-Assembled Long Co_3O_4 Hollow Tube Network with Multiple Heteroatom (C-, N- and S-) Doping. *J. Mater. Chem. A* **2016**, *4*, 9097−9105.
(51) Qorbani, M.; Chou, T.; Lee, Y.; Samireddi, S.; Naseri, N.; Ganguly, A.; Esfandiar, A.; Wang, C.; Chen, L.; Chen, K.; Moshfegh, A. Z. Multi-Porous Co3O4 Nanoflakes @ Sponge-Like Few-Layer Partially Reduced Graphene Oxide Hybrids: Towards Highly Stable Asymmetric Supercapacitors. *J. Mater. Chem. A* **2017**, *5*, 12569−12577.
(52) Xie, L.; Su, F.; Xie, L.; Li, X.; Liu, Z.; Kong, Q.; Guo, X.; Zhang, Y.; Wan, L.; Li, K.; Lv, C.; Chen, C. Self-Assembled 3D Graphene-Based Aerogel with Co_3O_4 Nanoparticles as High-Performance Asymmetric Supercapacitor Electrode. *ChemSusChem* **2015**, *8*, 2917−2926.
(53) Hsu, C.; Hu, C.; Wu, T.; Chen, J.; Rajkumar, M. How the Electrochemical Reversibility of a Battery-Type Material Affects the Charge Balance and Performances of Asymmetric Supercapacitors. *Electrochim. Acta* **2014**, *146*, 759−768.
(54) Wang, Z.; Liu, Y.; Gao, C.; Jiang, H.; Zhang, J. A porous $Co(OH)_2$ Material Derived from a MOF Template and Its Superior Energy Storage Performance for Supercapacitors. *J. Mater. Chem. A* **2015**, *3*, 20658−20663.
(55) Wang, B.; Liu, Q.; Han, J.; Zhang, X.; Wang, J.; Li, Z.; Yan, H.; Liu, L. Deft Dipping Combined with Electrochemical Reduction to Obtain 3D Electrochemical Reduction Graphene Oxide and Its Applications in Supercapacitors. *J. Mater. Chem. A* **2014**, *2*, 1137−1143.
(56) Liu, W.; Li, X.; Zhu, M.; He, X. High-Performance All-Solid State Asymmetric Supercapacitor based on Co_3O_4 Nanowires and Carbon Aerogel. *J. Power Sources* **2015**, *282*, 179−186.
(57) Xu, J.; Xiao, T.; Tan, X.; Xiang, P.; Jiang, L.; Wu, D.; Li, J.; Wang, S. A New Asymmetric Aqueous Supercapacitor: Co_3O_4 //Co_3O_4 @Polypyrrole. *J. Alloys Compd.* **2017**, *706*, 351−357.
(58) Liu, W.; Li, X.; Zhu, M.; He, X. High-Performance All-Solid State Asymmetric Supercapacitor Based on Co_3O_4 Nanowires and Carbon Aerogel. *J. Power Sources* **2015**, *282*, 179−186.
(59) Wu, Z.; Ren, W.; Wang, D.; Li, F.; Liu, B.; Cheng, H. High-Energy MnO_2 Nanowire/Graphene and Graphene Asymmetric Electrochemical Capacitors. *ACS Nano* **2010**, *4*, 5835−5842.
(60) Wang, R.; Yan, X.; Lang, J.; Zheng, Z.; Zhang, P. A Hybrid Supercapacitor Based on Flower-Like $Co(OH)_2$ and Urchin-Like VN Electrode Materials. *J. Mater. Chem. A* **2014**, *2*, 12724−12732.
(61) Wang, X.; Liu, W. S.; Lu, X.; Lee, P. S. Dodecyl Sulfate-Induced Fast Faradic Process in Nickel Cobalt Oxide-Reduced Graphite Oxide Composite Material and Its Application for Asymmetric Supercapacitor Device. *J. Mater. Chem.* **2012**, *22*, 23114−23119.
(62) Wang, X.; Sumboja, A.; Lin, M.; Yan, J.; Lee, P. S. Enhancing Electrochemical Reaction Sites in Nickel-Cobalt Layered Double Hydroxides on Zinc tin Oxide Nanowires: a Hybrid Material for an Asymmetric Supercapacitor Device. *Nanoscale* **2012**, *4*, 7266−7272.

DOI: 10.1021/acsami.7b10309
ACS Appl. Mater. Interfaces XXXX, XXX, XXX−XXX